Microscopic Picture of Electron-Phonon Interaction in Two-Dimensional Halide Perovskites

THE JOURNAL OF PHYSICAL CHEMISTRY Letters

pubs.acs.org/JPCL

Letter

Microscopic Picture of Electron–Phonon Interaction in Two-Dimensional Halide Perovskites

David Feldstein, Raül Perea-Causín,* Shuli Wang, Mateusz Dyksik, Kenji Watanabe, Takashi Taniguchi, Paulina Plochocka, and Ermin Malic

Cite This: *J. Phys. Chem. Lett.* 2020, 11, 9975–9982

Read Online

ACCESS | Metrics & More | Article Recommendations

ABSTRACT: Perovskites have attracted much attention due to their remarkable optical properties. While it is well established that excitons dominate their optical response, the impact of higher excitonic states and formation of phonon sidebands in optical spectra still need to be better understood. Here, we perform a theoretical study of excitonic properties of monolayered hybrid organic perovskites—supported by temperature-dependent photoluminescence measurements. Solving the Wannier equation, we obtain microscopic access to the Rydberg-like series of excitonic states including their wave functions and binding energies. Exploiting the generalized Elliot formula, we calculate the photoluminescence spectra demonstrating a pronounced contribution of a phonon sideband for temperatures up to 50 K, in agreement with experimental measurements. Finally, we predict temperature-dependent line widths of the three energetically lowest excitonic transitions and identify the underlying phonon-driven scattering processes.

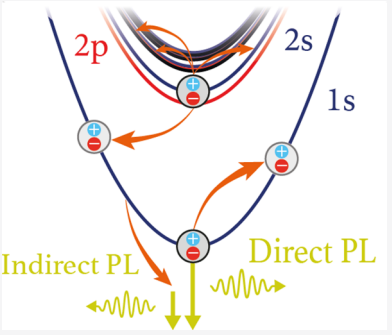

In the past years, much effort has been devoted to the study of perovskite materials.[1−5] Their broad absorption spectrum[6] combined with impressive light-emitting properties[7] makes them a promising material for optoelectronic applications. They have been, in particular, applied as active material in solar devices exhibiting a power conversion efficiency of up to 25.2%.[8] Beyond photovoltaics there has been a rising interest in perovskite-based diodes and lasers.[9−12] Recently, layered perovskites have emerged as a subclass of the bulk material exhibiting enhanced excitonic properties and tunable characteristics.[13] Their optical and electronic properties can be tailored through an external stress[14,15] or an internal chemical pressure[16] or by varying their layer thickness.[17] In addition, a wide variety of compositions can be made thanks to the large amount of organic cations that can be integrated into the structure. These materials are considered as a dimensional reduction of 3D perovskites with the general formula $(A)'_mA_{n-1}B_nX_{3n+1}$, where A′ is the cation that intercalates between the inorganic $A_{n-1}B_nX_{3n+1}$ layers and n can be understood as the thickness of the inorganic layers. Here, the screening of the Coulomb interaction is weaker compared to 3D perovskites, resulting in considerably larger exciton binding energies.[18,19] As a direct consequence, excitons play a crucial role in the optical response and nonequilibrium dynamics of these materials. Unbound carriers can still play a significant role at higher densities and excitations above the single-particle bandgap. Recent experimental studies on optical properties of 2D perovskites have focused on exciton binding energies,[19] absorption line widths,[12,20−24] phonon sidebands,[25] and high-density effects.[26] However, a microscopic understanding of some of the reported findings, for example, the formation of phonon sidebands and the microscopic origin of excitonic line widths, has not been well understood yet.

Here, we present a joint theoretical study of optical properties of monolayered hybrid organic perovskites supported by experimental photoluminescence (PL) measurements. The aim of the work is to provide a microscopic understanding of many-particle processes determining the temperature-dependent PL in these materials. We focus on the monolayered $(PEA)_2PbI_4$, which is a particular case of the n-layered $(PEA)_2MA_{n-1}Pb_nI_{3n+1}$ perovskite[27,28] (cf. Figure 1a). Here, the inorganic layer consists of corner-sharing PbI_6 octahedra sandwiched between two organic layers of PEA (phenylethylammonium). The lower dielectric constant of the organic layer results in a dielectrically confined quantum well.

Using a fully quantum mechanical approach, we obtain microscopic access to excitonic wave functions and binding energies in 2D perovskites. Exploiting the generalized Elliot formula, we model temperature-dependent PL spectra including the emergence of phonon-assisted sidebands. Finally, we determine the spectral line width of the energetically lowest

Received: August 31, 2020
Accepted: October 21, 2020
Published: November 12, 2020

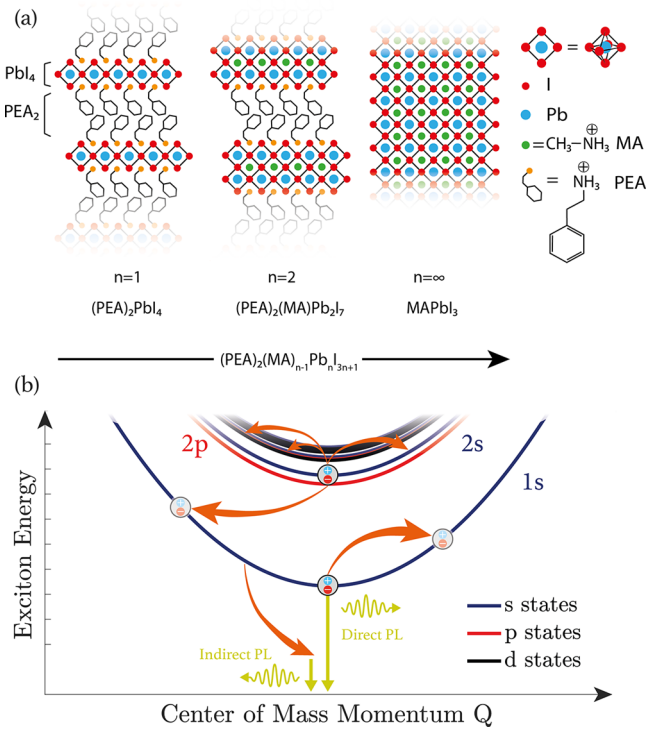

Figure 1. (a) Schematic illustration of the crystal structure of $(PEA)_2(MA)_{n-1}Pb_nI_{3n+1}$ from monolayered (n = 1) to bulk perovskites (n = ∞). (b) Exciton band structure and possible phonon-assisted scattering channels for 1s and 2s excitons.

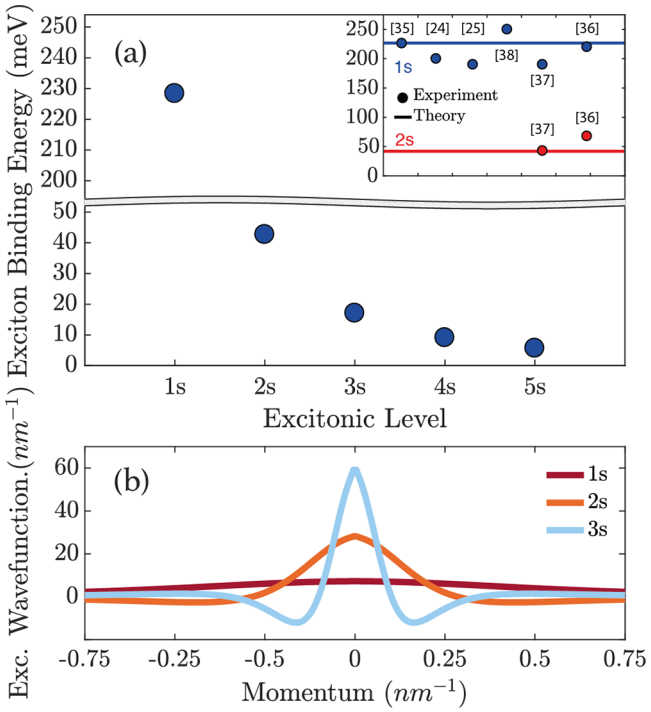

Figure 2. (a) Exciton binding energy of the energetically lowest s-type excitonic states in 2D perovskites. The inset shows a direct comparison to the measured values denoted by dots (and the corresponding references[24,25,35−38]). (b) Momentum-dependent wave functions for 1s, 2s, and 3s excitonic states.

excitonic transitions taking into account scattering channels driven by the emission and absorption of acoustic and optical phonons (cf. Figure 1b). The theoretical predictions are compared to temperature-dependent measurements of photoluminescence spectra in the investigated 2D perovskites.

As a first step, we determine the excitonic properties of monolayered $(PEA)_2PbI_4$ perovskites. To obtain microscopic access to the Rydberg-like series of excitonic states ν, their binding energies E_b^ν, and wave functions $\phi_{\mathbf{k}}^\nu$, we solve the Wannier equation[29−31]

$$\frac{\hbar^2\mathbf{k}^2}{2\mu}\phi_{\mathbf{k}}^{\nu} - \sum_{\mathbf{k}'} V_{|\mathbf{k}-\mathbf{k}'|}\phi_{\mathbf{k}'}^{\nu} = E_b^{\nu}\phi_{\mathbf{k}}^{\nu} \tag{1}$$

where we approximate the Coulomb interaction by the Rytova−Keldysh potential[32,33] $V_{\mathbf{q}} = \frac{e_0^2}{2\varepsilon_0\varepsilon_s L^2|\mathbf{q}|(1+r_0|\mathbf{q}|)}$ similar to the treatment of atomically thin transition metal dichalcogenides (TMDs).[34] Here, we used the exciton reduced mass[21] $\mu = 0.108m_0$ and the average dielectric constant[35] ε_s = 3.32 given by the organic layers. The dielectric constant of the inorganic layer is ε_{well} = 6.1, and its thickness is L_{well} = 0.636 nm.[35] These quantities determine the screening length $r_0 = L_{well}\frac{\varepsilon_{well}}{2\varepsilon_s}$, which is crucial for the excitonic binding energy E_b.

Evaluating the Wannier equation, we find E_b^{1s} = 228 meV for the energetically lowest 1s exciton state, while the binding energy decreases to 43 and 17 meV in the case of 2s and 3s states, respectively (cf. Figure 2a and Table 1). The obtained exciton binding energies are in good agreement with experimentally measured values (cf. the inset of Figure 2a). These experimental values have been determined by identifying the spectral position of the exciton resonances (1s and 2s) and the single-particle band edge in photoluminescence excitation,[25] optical absorption,[24,35,36] and electroabsorption[37] measurements or by extracting the thermal dissociation ratio of excitons from temperature-dependent photoluminescence measurements.[38] Note that interestingly the 2p state has a larger binding energy than the corresponding 2s state similarly to the case of TMD monolayers.[39] The corresponding eigenfunctions of the three lowest excitonic states are illustrated in Figure 2b and show the typical momentum dependence well known from the hydrogen problem.

Table 1. Excitonic Binding Energies E_b Obtained by Solving the Wannier Equation (cf. Eq 1)

excitonic state	E_{1s}	E_{2s}	E_{3s}	E_{4s}	E_{2p}	E_{3p}	E_{3d}
binding energy E_b [meV]	228	43	17	9	53	19.5	20

The obtained excitonic binding energies and wave functions will be used in the following to calculate the photoluminescence spectrum and the line widths of excitonic transitions in the investigated 2D perovskite material.

The photoluminescence is calculated by applying the density matrix formalism for an interacting system of electrons, phonons, and photons.[40−42] Using the Heisenberg equation of motion, we calculate the temporal evolution of the photon number $n_{\mathbf{k}} = \langle c_{\mathbf{k}}^\dagger c_{\mathbf{k}}\rangle$, which determines the photoluminescence via $I_{PL}(E) = \dot{n}_{\mathbf{k}}$.[31,43] Here, radiative and nonradiative decay channels play the crucial role. The radiative recombination of exciton states within the light cone is given by[44,45] $\gamma_{0\sigma}^{\nu} = \frac{\hbar e_0^2}{2m_0^2\varepsilon_0 n c_0}|M_\sigma|^2\frac{|\phi_\nu(\mathbf{r}=0)|^2}{E_0^\nu}$ with the excitonic resonance

https://dx.doi.org/10.1021/acs.jpclett.0c02661
J. Phys. Chem. Lett. 2020, 11, 9975−9982

energy $E_0^\nu = E_g + E_b^\nu$, the refractive index of the medium $n = \sqrt{\varepsilon_s} = 1.82$, and the optical matrix element for interband transitions $M_\sigma = 8$ fs eV nm^{-1} projected into the polarization σ of the emitted light. In the considered low-excitation regime, phonon-driven scattering channels determine the nonradiative dephasing[40,44]

$$\Gamma_{\mathbf{k}}^{\nu} = \pi \sum_{j,\mathbf{q},\pm,\mu} |G_{\mathbf{q}}^{\nu\mu j}|^2 \left(n_{\mathbf{q}}^{j} + \frac{1}{2} \pm \frac{1}{2}\right) \delta(\Delta E_{\mathbf{k},\mathbf{q}}^{\mu\nu,j}) \tag{2}$$

with $\Delta E_{\mathbf{k},\mathbf{q}}^{\mu\nu,j} = E_{\mathbf{k}+\mathbf{q}}^{\mu} - E_{\mathbf{k}}^{\nu} \pm \hbar\Omega_{\mathbf{q}}^{j}$. The excitonic dispersion $E_{\mathbf{k}}^{\nu}$ is described in an effective mass approximation with a total exciton mass $M = 0.44m_0$.[21] The equation includes absorption and emission ($\pm$) scattering channels involving acoustic and optical phonons with the mode j. The emission term (+) includes spontaneous and stimulated processes. The latter is proportional to the phonon occupation $n_{\mathbf{q}}^{j}$ that is given by the Bose−Einstein distribution within the considered bath approximation.

The appearing exciton−phonon matrix element $G_{\mathbf{q}}^{\nu\mu j} = \sum_{\mathbf{k}} \phi_{\mathbf{k}}^{\nu *}(\phi_{\mathbf{k}+\alpha_h\mathbf{q}}^{\mu} g_{\mathbf{q}}^{j,c} - \phi_{\mathbf{k}-\alpha_e\mathbf{q}}^{\mu} g_{\mathbf{q}}^{j,v})$ is given by the coupling elements for electrons and holes $g^{e/h}$ sandwiched by the exciton wave functions $\phi_{\mathbf{k}}^{\mu}$ of the involved initial and final exciton states with $\alpha_\lambda = m_\lambda/M$.[44,45] The electron−phonon coupling reads $g_{\mathbf{q}}^{j,\lambda} = D_{\mathbf{q}}^{j,\lambda}\left(\frac{\hbar^2}{2\rho\hbar\omega_{\mathbf{q}}^{j}}\right)^{1/2}$ with a constant deformation potential for optical phonons, i.e., $D_{\mathbf{q}}^{j,\lambda} = \pm D_{OP}^{j,\lambda}$, and with $D_{\mathbf{q}}^{j,\lambda} = \pm D_{AC}^{j,\lambda}|\mathbf{q}|$ for acoustic phonon modes.[46,47] The deformation potential interaction is equivalent to applying pressure or strain to the system,[47] resulting in energy shifts in opposite direction for conduction and valence bands. These energy shifts are reflected in the coupling strengths g^λ (note the $\pm$ signs in the deformation potentials defined above), and G is thus a result of adding the conduction (g^c) and valence (g^v) band terms. While the Fröhlich interaction dominates the electron−phonon interaction, its polar nature results in g^c and g^v having the same sign (as the energies shift in the same direction) and hence a weak exciton−phonon coupling strength G. First-principles studies are needed to obtain access to the full phonon dispersion and electron−phonon coupling elements as well as to thoroughly describe the importance of deformation potential and Fröhlich interactions. While this is beyond the scope of this work, we extract the values for deformation potentials from the experimentally measured temperature-dependent line width of the 1s exciton assuming one dominant optical and acoustic phonon branch (cf. Table 2). Note that these are effective modes that can contain several spectrally close phonon branches. We find that the linear increase of the PL line width at low temperatures can be traced back to the scattering with acoustic phonons characterized by the velocity $c_{AC} = 2100$ m/s. At high temperatures, there is a deviation from a linear increase and the major contribution stems from scattering with optical phonons exhibiting an energy of 35 meV, similar to recent experimental findings.[21,36,48] Note that there is also a defect-induced line width $\Gamma_0 = 6.7$ meV at zero temperature.

Table 2. Values for the Deformation Potentials for Optical and Acoustic Phonons Are Extracted from the Performed Measurements of Temperature-Dependent Excitonic Line Widths in PL Spectra Assuming One Dominant Optical and Acoustic Phonon Branch

D_{AC}	c_{AC}	D_{OP}	$\hbar\omega_{OP}$	Γ_0
1.9 eV	2100 m/s	158 eV/nm	35 meV	6.7 meV

Considering a many-particle Hamilton operator including exciton−photon and exciton−phonon interaction and evaluating the Heisenberg equation of motion for the photon number $n_{\mathbf{k}}$, we find a coupled set of differential equations including phonon- and photon-assisted polarizations. Then, the cluster expansion scheme[49] is used to factorize the many-particle expectation values disregarding contributions connected to multiphonon processes.[40] The final analytic expression for the σ-polarized photon flux emitted in perpendicular direction with respect to the monolayer is given by[40]

$$I_{PL,\sigma}(E) = \frac{2}{\hbar}|M_\sigma|^2 \sum_{\mu} \frac{|\phi^{\mu}(\mathbf{r}=0)|^2}{(E_0^{\mu} - E)^2 + (\gamma_{0,\sigma}^{\mu} + \Gamma_0^{\mu})^2} \times \left(\gamma_{0,\sigma}^{\mu} N_0^{\mu} + \sum_{\nu,\mathbf{q},j,\pm} |G_{\mathbf{q}}^{\nu\mu j}|^2 N_{\mathbf{q}}^{\nu} \eta_{j\mathbf{q}}^{\pm} \frac{\Gamma_{\mathbf{q}}^{\nu}}{(E_{\mathbf{q}}^{\nu} \mp \Omega_{\mathbf{q}}^{\alpha} - E)^2 + (\Gamma_{\mathbf{q}}^{\nu})^2}\right) \tag{3}$$

where $\eta_{j\mathbf{q}}^{\pm} = 1/2 \pm 1/2 + n_{\mathbf{q}}^{j}$ denotes the relevant phonon occupation factor for absorption/emission and $N_{\mathbf{q}}^{\nu}$ represents the exciton occupation corresponding to the Boltzmann distribution for the considered stationary PL. The first term describes the direct photoluminescence that is often termed zero-phonon contribution. The second term shows the phonon-assisted indirect PL and results in the emergence of phonon sidebands. Evaluating eq 3, we obtain a microscopic access to the temperature-dependent PL and find that the line width of the exciton transition clearly increases with temperature, while its intensity becomes smaller (cf. Figure 3a). The zero-phonon line width ranges between ∼5−10 meV at low temperatures and ∼50 meV at room temperature.

In Figure 3b−d, we decompose the direct PL stemming from radiative exciton recombination within the light cone ($\mathbf{Q} \approx 0$) from the indirect contribution to the PL arising from phonon-assisted exciton recombination from states with a nonzero center-of-mass momentum. We find a clear separation of the two contributions up to 50 K. At higher temperatures, the zero-phonon line becomes so broad that the phonon sideband is only visible as a low-energy shoulder. It becomes evident in an asymmetrically broadened exciton transition toward lower energies. The energetic separation of ∼35 meV between the zero-phonon line and the phonon sideband is governed by the energy of the involved optical phonons. In contrast, the weak contribution of phonon absorption leads to a negligible indirect photoluminescence on the high energy side of the zero-phonon line.

Optical phonons also govern the broadening of the zero-phonon line for temperatures above 100 K, while at lower temperature acoustic phonons dominate the PL line width, as will be further discussed later. The overall red-shift toward lower energies with decreasing temperature stems from a shift in the relative position of the conduction and valence bands due to polaronic effects[50] as well as the temperature-dependent contraction of the lattice. This phenomenon is known as the Varshni shift and can be described with the empirical formula[51] $E_g(T) = E_g(0) - \frac{\alpha_1 T^2}{\alpha_2 + T}$, where $E_g(0)$ is the band gap energy at

https://dx.doi.org/10.1021/acs.jpclett.0c02661
J. Phys. Chem. Lett. 2020, 11, 9975−9982

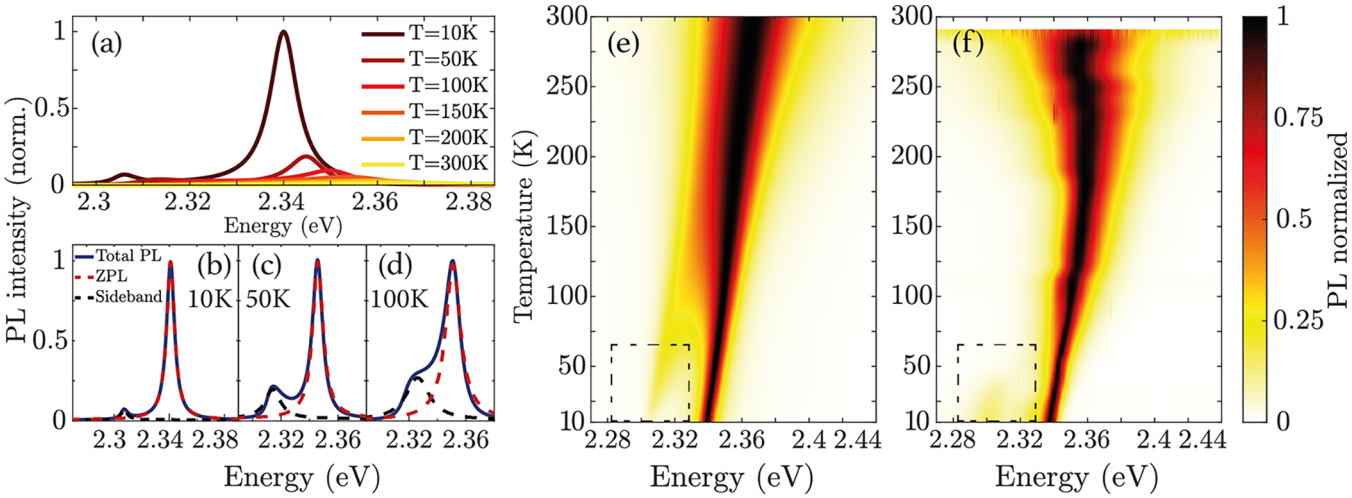

Figure 3. (a) Photoluminescence spectra of 2D perovskites shown at fixed temperatures. (b–d) PL decomposed into contributions stemming from the zero-phonon line (ZPL, dashed red) and the phonon sideband (dashed black) at three specific temperatures. (e) Theoretical prediction and (f) experimental measurement of the temperature- and energy-resolved PL with the phonon sideband appearing at low temperatures (rectangular box).

$T = 0$ K and α_1, α_2 are material-specific constants. The red-shift is treated phenomenologically in this work, and the material-specific constants are fitted to experimental data with $E_g(0) = 2.565$ eV.

To be able to directly compare the theoretical prediction to experiment, we have also performed temperature-dependent PL measurements of the same 2D perovskites. The experimental PL spectra were collected from a monocrystalline $(PEA)_2PbI_4$ thin sheet (~100 nm) exfoliated from chemically synthesized crystals. To provide better stability of the exfoliated perovskite layer, it was encapsulated by h-BN sheets (for more details see ref 21). For temperature-dependent PL measurements, the sample was mounted on the coldfinger of a helium flow cryostat with a quartz optical window. PL was excited with the frequency-doubled output of a mode-locked Ti-sapphire laser and tuned to 400 nm. The excitation laser beam was focused on the sample using a 50× microscope objective with a numerical aperture of 0.55, giving a spot size of ~1 μm diameter. The emitted PL was collected through the same objective and directed to a spectrometer equipped with a liquid nitrogen cooled charge-coupled device camera.

Figures 3e and 3f present a comparison of theoretically predicted and experimentally measured temperature- and energy-dependent PL spectra. We find a good qualitative agreement in terms of the appearance of the phonon sideband at the lower energy side of the zero-phonon line (cf. the rectangular boxes). In both experiment and theory, we find a pronounced phonon sideband appearing at 2.33 eV and staying clearly visible and distinguishable from the zero-phonon line for temperatures up to 50 K. Above this temperature the phonon sideband visible in experiment seems to merge/vanish with the main peak in contrast to theoretical predictions where this occurs around 100 K. We expect that this discrepancy can be related to h-BN encapsulation which might modify the motion of the inorganic layer and the related phonon mode with respect to the bulk case.[25] Indeed, in the case of the bulk $(PEA)_2PbI_4$ crystals the phonon sideband can be resolved up to around 100 K.[20] This observation may indicate that the electron–phonon interaction can be substantially modified in thin layers of 2D perovskites due to possible residual strain induced by the organic cation interacting with the encapsulating layer.[52] It is also worth to note that in encapsulated layers the LO phonon energy is slightly lower than in bulk samples[20,25,36] which also points to the non-negligible impact of encapsulation.

The spectral broadening of excitonic resonances with temperature plays an important role for the visibility of phonon sidebands. Thus, we study the exciton–phonon scattering channels determining the temperature-dependent spectral line width of the three energetically lowest excitonic transitions. The line width is determined on a microscopic footing within the second-order Born–Markov approximation resulting in the momentum-dependent scattering rates given in eq 2. The appearing sum over all phonon modes and momenta includes all scattering processes that fulfill the energy conservation, that is, $E^{\mu}_{\mathbf{k}+\mathbf{q}} - E^{\nu}_{\mathbf{k}} \pm \hbar\Omega^{j}_{\mathbf{q}} = 0$, where $\hbar\Omega^{j}_{\mathbf{q}}$ is the energy of the phonon with the mode j and momentum $\mathbf{q}$, while $E^{\nu}_{\mathbf{k}}$ and $E^{\mu}_{\mathbf{k}+\mathbf{q}}$ are the energies of the initial and final excitonic states. We include absorption (−) and emission (+) processes with optical and acoustic phonons. Because only the states within the light cone (i.e., $\mathbf{k} \approx 0$) contribute to the direct PL, the line width of the zero-phonon line is determined by the scattering rate $\Gamma^{\nu}_{\mathbf{k}\approx 0}$ (cf. Figure 1b).

The resulting line widths and their underlying microscopic scattering channels are displayed in Figure 4. We find spectral line widths of approximately 50, 25, and 15 meV for 1s, 2s, and 3s transitions at room temperature, respectively. In the case of 1s, we show that the scattering with acoustic phonons dominates the line width up to temperatures of ~150 K (cf. the orange shaded region in Figure 4a). We find a linear dependence on temperature reflecting the behavior of the phonon occupations that are described by the Bose–Einstein distribution. Optical phonons start to be important for temperatures above 100 K (red region) and become the main channel governing the line width of 1s from ~150 K. Optical phonons are important only at higher temperatures, since their energy is 35 meV, and thus the phonon occupation is negligibly small at low temperatures. There is also a temperature-independent contribution stemming from radiative recombination (gray region, 2.66 meV) that also limits the lifetime of 1s excitons in the light cone. The oscillator strength considerably decreases for higher transitions due to more spatially extended wave functions. Hence, the radiative

https://dx.doi.org/10.1021/acs.jpclett.0c02661
J. Phys. Chem. Lett. 2020, 11, 9975–9982

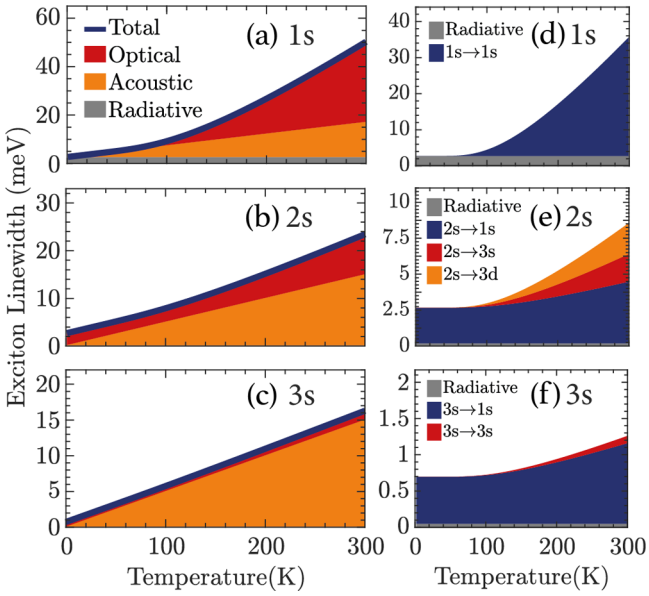

Figure 4. (a–c) Temperature-dependent exciton line width of the three energetically lowest excitonic transitions (1s, 2s, and 3s) resolving the contribution of optical and acoustic phonons. (d–f) Microscopic scattering channels driven by optical phonons for the considered excitonic transitions.

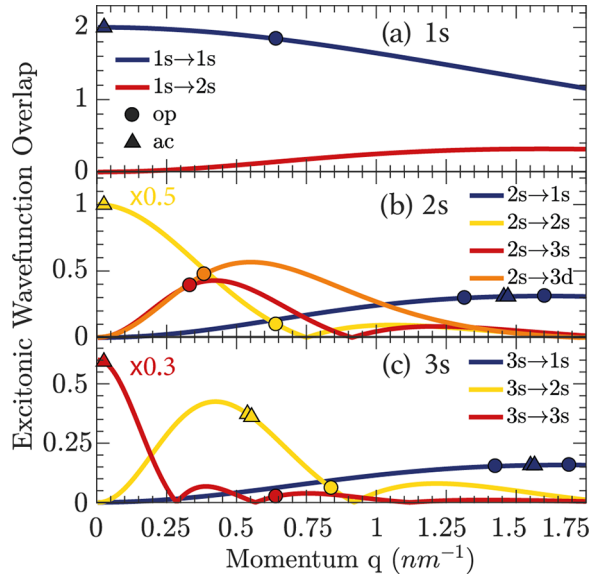

Figure 5. Wave function overlap of the excitonic states involved in phonon-driven transitions, which determine the spectral line width of (a) 1s, (b) 2s, and (c) 3s states. The circular (triangular) markers indicate the momentum at which the scattering can take place via optical (acoustic) phonons. Here, the energy conservation is fulfilled. Note that the strongest wave function overlap involving the transitions within the same band have been multiplied by a factor of 0.5 or 0.3 to be able to better illustrate other scattering channels.

recombination has only a marginal contribution to their line widths with 1.9×10^{-1} meV for 2s and 4.9×10^{-2} meV for 3s (cf. Figure 4b,c). Note that we assume an ideal defect-free sample by disregarding the constant broadening Γ_0 that arises from scattering with defects and does not have any impact on the investigated temperature dependence.

The quasi-linear dependence of the line width for higher states (2s and 3s) is caused by the fact that scattering with acoustic phonons is the main mechanism limiting the lifetime of 2s and 3s states at all temperatures. To explain the overall low importance of optical phonons for higher excitonic states, we investigate the wave function overlap $\sum_{k,\alpha} \phi^{\nu^*}_{\mathbf{k}} \phi^{\mu}_{\mathbf{k}+\alpha\mathbf{q}}$ of the involved initial and final scattering states that enters in the exciton–phonon coupling elements. In particular, it is important to consider the specific momenta where energy conservation is fulfilled (cf. circular and triangular markers in Figure 5 denoting these momenta for optical and acoustic phonons, respectively). We find that the only possible scattering channel fulfilling the energy conservation for the 1s exciton is the intraband 1s → 1s scattering with optical and acoustic phonons, as shown in Figure 4d.

For the higher 2s and 3s states, multiple scattering channels are possible (cf. Figure 5b,c). Nevertheless, in all three cases it is the intraband scattering with acoustic phonons that shows the maximum wave function overlap due to the small momentum transfer of this transition. To be able to explain which specific scattering channel and phonon mode dominate the line width, it is not always sufficient to only consider the wave function overlap. The exciton–phonon coupling element is determined by the wave function overlap weighted by the corresponding deformation potential that is constant for optical phonons and linear in $\mathbf{q}$ for acoustic phonons. Furthermore, the temperature- and energy-dependent occupation of the involved phonon modes also needs to be considered since it directly enters the scattering rate (cf. eq 2). The combination of a strong electron–phonon coupling, large wave function overlap, and a moderate phonon number results in a very efficient intraband scattering with acoustic phonons that dominates the line width. The efficiency of scattering with optical phonons decreases for higher states despite the enhanced number of possible scattering channels—as already seen in transition metal dichalcogenides.[45] This can be traced back to lower excitonic binding energies and thus more spatially extended excitonic wave functions. Because scattering with optical phonons provides a higher energy and momentum exchange than with acoustic phonons, the scattering strength will be determined by the overlap of two wave functions with significantly different momenta. Because the wave functions of higher excitonic states are more localized in momentum space, there is only a small overlap of initial and final state wave functions giving rise to a large suppression of scattering processes with optical phonons.

While acoustic phonons predominantly induce scattering within an excitonic band, optical phonons can also bridge larger energy distances between different bands. To better understand these processes, we further decompose the most important scattering channels with optical phonons in Figure 4d–f. Because for optical phonons the coupling strength and phonon number do not depend on momentum, the efficiency of a particular scattering channel is only determined by the wave function overlap. We find that the most important contribution caused by optical phonons corresponds to emission processes to the energetically lower 1s state (blue areas in Figure 4e,f). Note that spontaneous emission is much more likely than stimulated emission at low temperatures, where the phonon number is very small. Moreover, the fact that spontaneous emission does not depend on the phonon number results in the constant line width at low temperatures. For 2s excitons, the wave function overlap for the optical phonon absorption processes 2s → 3s and 2s → 3d stands out

https://dx.doi.org/10.1021/acs.jpclett.0c02661
J. Phys. Chem. Lett. 2020, 11, 9975–9982

(cf. Figure 5b), which is directly reflected in their important contributions to the optical phonon portion of the line width in Figure 4e.

The 3s exciton state is close to the continuum allowing multiple scattering channels driven by emission and absorption of phonons. The scattering with optical phonons at the 3s state is dominated by the 3s → 1s transition induced by spontaneous emission (cf. Figure 4f). Furthermore, because of the energetic proximity of other states, significant wave function overlap exists for interband acoustic phonon scattering processes (cf. Figure 5c). However, the small phonon number at the large momenta involved in these scattering processes drastically reduces the efficiency of these channels, resulting in an even smaller line width at room temperature compared to the 1s exciton exhibiting much fewer scattering channels.

In summary, we have presented a theoretical study supported by experimental measurements shining light on excitonic properties of monolayered halide perovskites. On the basis of a quantum mechanical approach, we have determined the eigenfunctions and binding energies of the entire Rydberg-like series of excitonic states. Furthermore, we have calculated and measured temperature-dependent photoluminescence spectra with a particular focus on the emergence of low-energy phonon sidebands. Finally, we have provided microscopic insights into the exciton−phonon scattering channels governing the temperature-dependent spectral line width of the three energetically lowest excitonic transitions. Overall, our work contributes to a better understanding of the optical properties of 2D perovskites and can guide future studies in this growing field of research.

AUTHOR INFORMATION

Corresponding Author

Raül Perea-Causín − *Department of Physics, Chalmers University of Technology, Gothenburg 412 96, Sweden;* orcid.org/0000-0002-2229-0147; Email: causin@chalmers.se

Authors

David Feldstein − *Department of Physics, Chalmers University of Technology, Gothenburg 412 96, Sweden; Campus Nord, Universitat Politècnica de Catalunya, Barcelona 08034, Spain*

Shuli Wang − *UPR 3228, CNRS-UGA-UPS-INSA, Laboratoire National des Champs Magnétiques Intenses, Grenoble and Toulouse, France*

Mateusz Dyksik − *UPR 3228, CNRS-UGA-UPS-INSA, Laboratoire National des Champs Magnétiques Intenses, Grenoble and Toulouse, France; Department of Experimental Physics, Faculty of Fundamental Problems of Technology, Wroclaw University of Science and Technology, Wroclaw, Poland;* orcid.org/0000-0003-4945-8795

Kenji Watanabe − *Research Center for Functional Materials, National Institute for Materials Science, Tsukuba 305-0044, Japan;* orcid.org/0000-0003-3701-8119

Takashi Taniguchi − *Research Center for Functional Materials, National Institute for Materials Science, Tsukuba 305-0044, Japan;* orcid.org/0000-0002-1467-3105

Paulina Plochocka − *UPR 3228, CNRS-UGA-UPS-INSA, Laboratoire National des Champs Magnétiques Intenses, Grenoble and Toulouse, France; Department of Experimental Physics, Faculty of Fundamental Problems of Technology, Wroclaw University of Science and Technology, Wroclaw, Poland;* orcid.org/0000-0002-4019-6138

Ermin Malic − *Department of Physics, Chalmers University of Technology, Gothenburg 412 96, Sweden*

Complete contact information is available at: https://pubs.acs.org/10.1021/acs.jpclett.0c02661

Notes

The authors declare no competing financial interest.

ACKNOWLEDGMENTS

We thank Alexey Chernikov and Jonas D. Ziegler (University of Regensburg) for providing the samples and helping analyze the obtained results. Furthermore, we thank Samuel Brem (Chalmers University of Technology) for discussions on modeling PL spectra. This project has received funding from the Swedish Research Council (VR, project number 2018-00734) and the European Union's Horizon 2020 research and innovation programme under grant agreement no. 881603. The computations were enabled by resources provided by the Swedish National Infrastructure for Computing (SNIC) at C3SE partially funded by the Swedish Research Council through grant agreement no. 2016-07213. R.P.C. acknowledges funding from the Excellence Initiative Nano (Chalmers) under the Excellence PhD programme. P.P. appreciates support from National Science Centre Poland within the OPUS program (grant no. 2019/33/B/ST3/01915). This work was partially supported by the OPEP project, which received funding from the ANR-10-LABX-0037-NEXT. M.D. appreciates support from the Polish National Agency for Academic Exchange within the Bekker programme (grant no. PPN/BEK/2019/1/00312/U/00001). The Polish participation in EMFL is supported by the DIR/WK/2018/07 grant from Polish Ministry of Science and Higher Education. K.W. and T.T. acknowledge support from the Elemental Strategy Initiative conducted by the MEXT, Japan, under grant nos. JPMXP0112101001, JSPS KAKENHI, and JP20H00354 and the CREST (no. JPMJCR15F3), JST.

REFERENCES

(1) Jena, A. K.; Kulkarni, A.; Miyasaka, T. Halide Perovskite Photovoltaics: Background, Status, and Future Prospects. *Chem. Rev.* **2019**, *119*, 3036−3103.

(2) Stoumpos, C. C.; Malliakas, C. D.; Kanatzidis, M. G. Semiconducting Tin and Lead Iodide Perovskites with Organic Cations: Phase Transitions, High Mobilities, and Near-Infrared Photoluminescent Properties. *Inorg. Chem.* **2013**, *52*, 9019−9038.

(3) Niu, G.; Guo, X.; Wang, L. Review of Recent Progress in Chemical Stability of Perovskite Solar Cells. *J. Mater. Chem. A* **2015**, *3*, 8970−8980.

(4) Yin, W.-J.; Yang, J.-H.; Kang, J.; Yan, Y.; Wei, S.-H. Halide Perovskite Materials for Solar Cells: A Theoretical Review. *J. Mater. Chem. A* **2015**, *3*, 8926−8942.

(5) Tsai, H.; Nie, W.; Blancon, J.-C.; Stoumpos, C. C.; Asadpour, R.; Harutyunyan, B.; Neukirch, A. J.; Verduzco, R.; Crochet, J. J.; Tretiak, S.; et al. High-Efficiency two-dimensional Ruddlesden−Popper Perovskite Solar Cells. *Nature* **2016**, *536*, 312−316.

(6) Hao, F.; Stoumpos, C. C.; Chang, R. P. H.; Kanatzidis, M. G. Anomalous Band Gap Behavior in Mixed Sn and Pb Perovskites Enables Broadening of Absorption Spectrum in Solar Cells. *J. Am. Chem. Soc.* **2014**, *136*, 8094−8099.

(7) Adjokatse, S.; Fang, H.-H.; Loi, M. A. Broadly Tunable Metal Halide Perovskites for Solid-State Light-Emission Applications. *Mater. Today* **2017**, *20*, 413−424.

(8) Huang, J.; Shao, Y.; Dong, Q. Organometal Trihalide Perovskite Single Crystals: A Next Wave of Materials for 25% Efficiency Photovoltaics and Applications Beyond? *J. Phys. Chem. Lett.* **2015**, *6*, 3218−3227.
(9) Tan, Z.-K.; Moghaddam, R. S.; Lai, M. L.; Docampo, P.; Higler, R.; Deschler, F.; Price, M.; Sadhanala, A.; Pazos, L. M.; Credgington, D.; et al. Bright Light-Emitting Diodes Based on Organometal Halide Perovskite. *Nat. Nanotechnol.* **2014**, *9*, 687−692.
(10) Cho, H.; Jeong, S.-H.; Park, M.-H.; Kim, Y.-H.; Wolf, C.; Lee, C.-L.; Heo, J. H.; Sadhanala, A.; Myoung, N.; Yoo, S.; et al. Overcoming the Electroluminescence Efficiency Limitations of Perovskite Light-Emitting Diodes. *Science* **2015**, *350*, 1222−1225.
(11) Matsushima, T.; Bencheikh, F.; Komino, T.; Leyden, M. R.; Sandanayaka, A. S. D.; Qin, C.; Adachi, C. High Performance from Extraordinarily Thick Organic Light-Emitting Diodes. *Nature* **2019**, *572*, 502−506.
(12) Gong, X.; Voznyy, O.; Jain, A.; Liu, W.; Sabatini, R.; Piontkowski, Z.; Walters, G.; Bappi, G.; Nokhrin, S.; Bushuyev, O.; et al. Electron−Phonon Interaction in Efficient Perovskite Blue Emitters. *Nat. Mater.* **2018**, *17*, 550−556.
(13) Mao, L.; Stoumpos, C. C.; Kanatzidis, M. G. Two-Dimensional Hybrid Halide Perovskites: Principles and Promises. *J. Am. Chem. Soc.* **2019**, *141*, 1171−1190.
(14) Mante, P.-A.; Stoumpos, C. C.; Kanatzidis, M. G.; Yartsev, A. Electron−Acoustic Phonon Coupling in Single Crystal CH3NH3PbI3 Perovskites Revealed by Coherent Acoustic Phonons. *Nat. Commun.* **2017**, *8*, 14398.
(15) Lü, X.; Yang, W.; Jia, Q.; Xu, H. Pressure-Induced Dramatic Changes in Organic−Inorganic Halide Perovskites. *Chem. Sci.* **2017**, *8*, 6764−6776.
(16) Sun, S.; Fang, Y.; Kieslich, G.; White, T. J.; Cheetham, A. K. Mechanical Properties of Organic−Inorganic Halide Perovskites, CH3NH3PbX3 (X = I, Br and Cl), by Nanoindentation. *J. Mater. Chem. A* **2015**, *3*, 18450−18455.
(17) Etgar, L. The Merit of Perovskite's Dimensionality; Can this Replace the 3D Halide Perovskite? *Energy Environ. Sci.* **2018**, *11*, 234−242.
(18) Milot, R. L.; Sutton, R. J.; Eperon, G. E.; Haghighirad, A. A.; Martinez Hardigree, J.; Miranda, L.; Snaith, H. J.; Johnston, M. B.; Herz, L. M. Charge-Carrier Dynamics in 2D Hybrid Metal−Halide Perovskites. *Nano Lett.* **2016**, *16*, 7001−7007.
(19) Yaffe, O.; Chernikov, A.; Norman, Z. M.; Zhong, Y.; Velauthapillai, A.; van der Zande, A.; Owen, J. S.; Heinz, T. F. Excitons in Ultrathin Organic-Inorganic Perovskite Crystals. *Phys. Rev. B: Condens. Matter Mater. Phys.* **2015**, *92*, 045414.
(20) Straus, D. B.; Iotov, N.; Gau, M. R.; Zhao, Q.; Carroll, P. J.; Kagan, C. R. Longer Cations Increase Energetic Disorder in Excitonic 2D Hybrid Perovskites. *J. Phys. Chem. Lett.* **2019**, *10*, 1198−1205.
(21) Ziegler, J. D.; Zipfel, J.; Meisinger, B.; Menahem, M.; Zhu, X.; Taniguchi, T.; Watanabe, K.; Yaffe, O.; Egger, D. A.; Chernikov, A. Fast and Anomalous Exciton Diffusion in Two-Dimensional Hybrid Perovskites. *Nano Lett.* **2020**, *20*, 6674−6681.
(22) Guo, Z.; Wu, X.; Zhu, T.; Zhu, X.; Huang, L. Electron−Phonon Scattering in Atomically Thin 2D Perovskites. *ACS Nano* **2016**, *10*, 9992−9998.
(23) Ni, L.; Huynh, U.; Cheminal, A.; Thomas, T. H.; Shivanna, R.; Hinrichsen, T. F.; Ahmad, S.; Sadhanala, A.; Rao, A. Real-Time Observation of Exciton−Phonon Coupling Dynamics in Self-Assembled Hybrid Perovskite Quantum Wells. *ACS Nano* **2017**, *11*, 10834−10843.
(24) Gauthron, K.; Lauret, J-S.; Doyennette, L.; Lanty, G.; Al Choueiry, A.; Zhang, S. J.; Brehier, A.; Largeau, L.; Mauguin, O.; Bloch, J.; Deleporte, E. Optical Spectroscopy of Two-Dimensional Layered (C_6H_5C2H4-NH3)2-PbI4 Perovskite. *Opt. Express* **2010**, *18*, 5912−5919.
(25) Straus, D. B.; Hurtado Parra, S.; Iotov, N.; Gebhardt, J.; Rappe, A. M.; Subotnik, J. E.; Kikkawa, J. M.; Kagan, C. R. Direct Observation of Electron−Phonon Coupling and Slow Vibrational Relaxation in Organic−Inorganic Hybrid Perovskites. *J. Am. Chem. Soc.* **2016**, *138*, 13798−13801.
(26) Palmieri, T.; Baldini, E.; Steinhoff, A.; Akrap, A.; Kollár, M.; Horváth, E.; Forró, L.; Jahnke, F.; Chergui, M. Mahan Excitons in Room-Temperature Methylammonium Lead Bromide Perovskites. *Nat. Commun.* **2020**, *11*, 1−8.
(27) Calabrese, J.; Jones, N. L.; Harlow, R. L.; Herron, N.; Thorn, D. L.; Wang, Y. Preparation and Characterization of Layered Lead Halide Compounds. *J. Am. Chem. Soc.* **1991**, *113*, 2328−2330.
(28) Smith, I. C.; Hoke, E. T.; Solis-Ibarra, D.; McGehee, M. D.; Karunadasa, H. I. A Layered Hybrid Perovskite Solar-Cell Absorber with Enhanced Moisture Stability. *Angew. Chem., Int. Ed.* **2014**, *53*, 11232−11235.
(29) Koch, S. W.; Kira, M.; Khitrova, G.; Gibbs, H. M. Semiconductor Excitons in New Light. *Nat. Mater.* **2006**, *5*, 523−531.
(30) Brem, S.; Selig, M.; Berghaeuser, G.; Malic, E. Exciton Relaxation Cascade in two-dimensional Transition Metal Dichalcogenides. *Sci. Rep.* **2018**, *8*, 8238.
(31) Selig, M.; Berghäuser, G.; Richter, M.; Bratschitsch, R.; Knorr, A.; Malic, E. Dark and Bright Exciton Formation, Thermalization, and Photoluminescence in Monolayer Transition Metal Dichalcogenides. *2D Mater.* **2018**, *5*, 035017.
(32) Rytova, N. S. The Screened Potential of a Point Charge in a Thin Film. *Moscow Univ. Phys. Bull.* **1967**, *3*, 18.
(33) Keldysh, L. V. Coulomb Interaction in Thin Semiconductor and Semimetal films. *JETP Lett.* **1979**, *29*, 658.
(34) Berghäuser, G.; Malic, E. Analytical Approach to Excitonic Properties of MoS_2. *Phys. Rev. B: Condens. Matter Mater. Phys.* **2014**, *89*, 125309.
(35) Hong, X.; Ishihara, T.; Nurmikko, A. V. Dielectric Confinement Effect on Excitons in PbI_4-based Layered Semiconductors. *Phys. Rev. B: Condens. Matter Mater. Phys.* **1992**, *45*, 6961−6964.
(36) Urban, J. M.; Chehade, G.; Dyksik, M.; Menahem, M.; Surrente, A.; Trippe-Allard, G.; Maude, D. K.; Garrot, D.; Yaffe, O.; Deleporte, E.; Plochocka, P.; Baranowski, M. Revealing Excitonic Phonon Coupling in (PE) 2 (MA) n- 1PbnI3n+ 12D Layered Perovskites. *J. Phys. Chem. Lett.* **2020**, *11*, 5830.
(37) Zhai, Y.; Baniya, S.; Zhang, C.; Li, J.; Haney, P.; Sheng, C.-X.; Ehrenfreund, E.; Vardeny, Z. V. Giant Rashba Splitting in 2D Organic-Inorganic Halide Perovskites Measured by Transient Spectroscopies. *Sci. Adv.* **2017**, *3*, e1700704.
(38) Cheng, B.; Li, T.-Y.; Maity, P.; Wei, P.-C.; Nordlund, D.; Ho, K.-T.; Lien, D.-H.; Lin, C.-H.; Liang, R.-Z.; Miao, X.; et al. Extremely Reduced Dielectric Confinement in Two-Dimensional Hybrid Perovskites With Large Polar Organics. *Commun. Phys.* **2018**, *1*, 80.
(39) Berghäuser, G.; Knorr, A.; Malic, E. Optical Fingerprint of Dark 2p-States in Transition Metal Dichalcogenides. *2D Mater.* **2017**, *4*, 015029.
(40) Brem, S.; Ekman, A.; Christiansen, D.; Katsch, F.; Selig, M.; Robert, C.; Marie, X.; Urbaszek, B.; Knorr, A.; Malic, E. Phonon-Assisted Photoluminescence from Indirect Excitons in Monolayers of Transition-Metal Dichalcogenides. *Nano Lett.* **2020**, *20*, 2849−2856.
(41) Malic, E.; Knorr, A. *Graphene and Carbon Nanotubes: Ultrafast Optics and Relaxation Dynamics*; Wiley-VHC: Berlin, 2013.
(42) Kadi, F.; Winzer, T.; Malic, E.; Knorr, A.; Göttfert, F.; Mittendorff, M.; Winnerl, S.; Helm, M. Microscopic Description of Intraband Absorption in Graphene: the Occurrence of Transient Negative Differential Transmission. *Phys. Rev. Lett.* **2014**, *113*, 035502.
(43) Kira, M.; Jahnke, F.; Hoyer, W.; Koch, S. Quantum Theory of Spontaneous Emission and Coherent Effects in Semiconductor Microstructures. *Prog. Quantum Electron.* **1999**, *23*, 189−279.
(44) Selig, M.; Berghäuser, G.; Raja, A.; Nagler, P.; Schüller, C.; Heinz, T. F.; Korn, T.; Chernikov, A.; Malic, E.; Knorr, A. Excitonic Linewidth and Coherence Lifetime in Monolayer Transition Metal Dichalcogenides. *Nat. Commun.* **2016**, *7*, 13279.
(45) Brem, S.; Zipfel, J.; Selig, M.; Raja, A.; Waldecker, L.; Ziegler, J. D.; Taniguchi, T.; Watanabe, K.; Chernikov, A.; Malic, E. Intrinsic

https://dx.doi.org/10.1021/acs.jpclett.0c02661
J. Phys. Chem. Lett. 2020, 11, 9975−9982

Lifetime of Higher Excitonic States in Tungsten Diselenide Monolayers. *Nanoscale* **2019**, *11*, 12381−12387.
(46) Kaasbjerg, K.; Thygesen, K. S.; Jacobsen, K. W. Phonon-Limited Mobility in *n*-type Single-Layer MoS_2 from First Principles. *Phys. Rev. B: Condens. Matter Mater. Phys.* **2012**, *85*, 115317.
(47) Mahan, G. D. *Many-Particle Physics*; Springer: New York, 2013.
(48) Zhang, Y.; Wang, R.; Li, Y.; Wang, Z.; Hu, S.; Yan, X.; Zhai, Y.; Zhang, C.; Sheng, C. Optical Properties of Two-Dimensional Perovskite Films of $(C_6H_5C2H4NH3)$ 2 [PbI4] and $(C_6H_5C2H4NH3)$ 2 (CH3NH3) 2 [Pb3I10]. *J. Phys. Chem. Lett.* **2019**, *10*, 13−19.
(49) Kira, M.; Koch, S. Many-Body Correlations and Excitonic Effects in Semiconductor Spectroscopy. *Prog. Quantum Electron.* **2006**, *30*, 155−296.
(50) Christiansen, D.; Selig, M.; Berghäuser, G.; Schmidt, R.; Niehues, I.; Schneider, R.; Arora, A.; de Vasconcellos, S. M.; Bratschitsch, R.; Malic, E.; et al. Phonon Sidebands in Monolayer Transition Metal Dichalcogenides. *Phys. Rev. Lett.* **2017**, *119*, 187402.
(51) Varshni, Y. Temperature Dependence of the Energy Gap in Semiconductors. *Physica* **1967**, *34*, 149−154.
(52) Du, Q.; Zhu, C.; Yin, Z.; Na, G.; Cheng, C.; Han, Y.; Liu, N.; Niu, X.; Zhou, H.; Chen, H.; et al. Stacking Effects on Electron−Phonon Coupling in Layered Hybrid Perovskites via Microstrain Manipulation. *ACS Nano* **2020**, *14*, 5806−5817.

https://dx.doi.org/10.1021/acs.jpclett.0c02661
J. Phys. Chem. Lett. 2020, 11, 9975−9982